PhotoniX

RESEARCH Open Access

Visualizing cortical blood perfusion after photothrombotic stroke in vivo by needle-shaped beam optical coherence tomography angiography

Xiangyu Guo[1†], Jingjing Zhao[2,9†], Liqun Sun[1], Varun Gupta[3], Lin Du[5], Komal Sharma[2], Aidan Van Vleck[2], Kaitlyn Liang[4], Liangcai Cao[1], Lingjie Kong[1], Yuanmu Yang[1], Yong Huang[6*], Adam de la Zerda[2,7,8*] and Guofan Jin[1*]

†Xiangyu Guo and Jingjing Zhao contributed equally to this work.

*Correspondence: huangyong2015@bit.edu.cn; adlz@stanford.edu; jgf-dpi@mail.tsinghua.edu.cn

[1] State Key Laboratory of Precision Measurement Technology and Instruments, Department of Precision Instrument, Tsinghua University, Beijing 100084, China
[2] Department of Structural Biology, Stanford University School of Medicine, Stanford University, Stanford, CA 94305, USA
[6] School of Optics and Photonics, Beijing Institute of Technology, No. 5 South Zhongguancun Street, Haidian, Beijing 100081, China
Full list of author information is available at the end of the article

Abstract

Optical imaging techniques provide low-cost, non-radiative images with high spatiotemporal resolution, making them advantageous for long-term dynamic observation of blood perfusion in stroke research and other brain studies compared to non-optical methods. However, high-resolution imaging in optical microscopy fundamentally requires a tight optical focus, and thus a limited depth of field (DOF). Consequently, large-scale, non-stitched, high-resolution images of curved surfaces, like brains, are difficult to acquire without z-axis scanning. To overcome this limitation, we developed a needle-shaped beam optical coherence tomography angiography (NB-OCTA) system, and for the first time, achieved a volumetric resolution of less than 8 μm in a non-stitched volume space of 6.4 mm × 4 mm × 620 μm in vivo. This system captures the distribution of blood vessels at 3.4-times larger depths than normal OCTA equipped with a Gaussian beam (GB-OCTA). We then employed NB-OCTA to perform long-term observation of cortical blood perfusion after stroke in vivo, and quantitatively analyzed the vessel area density (VAD) and the diameters of representative vessels in different regions over 10 days, revealing different spatiotemporal dynamics in the acute, sub-acute and chronic phase of post-ischemic revascularization. Benefiting from our NB-OCTA, we revealed that the recovery process is not only the result of spontaneous reperfusion, but also the formation of new vessels. This study provides visual and mechanistic insights into strokes and helps to deepen our understanding of the spontaneous response of brain after stroke.

Keywords: Optical coherence tomography angiography, Diffractive optical elements, Needle-shaped beam, Brain imaging, Stroke, Cortical blood perfusion

Introduction

Stroke is the second highest cause of death globally and a leading cause of disability. It has shown increasing incidence in developing countries, where 70% strokes are of ischemic origin [1]. Due to its widespread prevalence and limited therapeutic

management options, ongoing stroke research revolves around investigation of several therapeutic interventions in preclinical and clinical settings. Animal models have been extensively used in preclinical research [2, 3], and three commonly used methods to model experimental stroke include craniectomy models [4], intraluminal suture [5], and photothrombotic (PT) stroke model [6, 7]. Craniectomy models involve invasive clipping, ligation or electrocoagulation techniques that can cause mechanical damage to the cortex, and intraluminal suture models require a high-level of surgical expertise and may not generate reproducible ischemic lesions. Contrastingly, the PT stroke model has gained wide acceptance due to its precise spatial controllability, which allows targeting of any cortical region of interest in a reproducible and minimally invasive manner [8].

Although the research on the pathological mechanisms of ischemic stroke has made progress [9, 10], clinical treatment options and drug development still remain challenging. Quick and effective restoration of cerebral blood flow can arrest pathological events and reduce functional damage [11]. Therefore, thrombolysis is critical in early treatment of ischemic stroke [12, 13], with an optimal window of 4.5 h after ischemia [14], but most patients do not catch this time window. In addition to natural and interventional revascularization, localized spontaneous vascular regeneration, or angiogenesis can occur. Angiogenesis is triggered by hypoxia as oxygen deficiency upregulates proangiogenic factors [15]. This results in the subsequent upregulation of hypoxia-inducible factors, followed by the expression of angiopoietin, erythropoietin, nitric oxide synthase, vascular endothelial growth factor (VEGF) and their receptors [16]. Angiogenesis is also believed to occur in the adult brain, but this process remains largely unexplored [17, 18]. Hence, a rapid, high-resolution, in vivo imaging technique might be a vital asset in both visually assessing blood perfusion and brain tissue damage, and longitudinal monitoring of the ischemic area to study the mechanisms of post-stroke revascularization.

Magnetic resonance imaging (MRI) and computed tomography (CT) are commonly used brain imaging modalities in clinical practice [19, 20]. MRI has a high sensitivity and specificity for detecting pathological changes such as cerebral vessels, lesions, and tumors, but repeated MRI scans can be expensive and time consuming. CT provides fast and high-quality images, but frequent measurements involve high levels of radiation exposure. While these non-optical imaging methods can achieve a large imaging depth, their resolution is limited to the sub-millimeter level.

Resultingly, optical imaging techniques are becoming a popular choice for brain studies due to their high spatial and temporal resolution [8, 21, 22]. Researchers have demonstrated an increasing impact on brain imaging by using photoacoustic microscopy (PAM) [21], which can measure blood flow and oxygen metabolism by detecting endogenous and exogenous contrasts [23]. However, PAM requires water as the coupling medium for ultrasound transmission, making the system more complex. Two-photon (2P) microscopy, allows subcellular image resolution and imaging depths of several hundred micrometers into living brain tissue [24], but 2P microscopy observations of stroke models may permit dye leakage thus impeding microvasculature imaging due to ischemic damage to the cortical tissue [25]. It would therefore be particularly useful for stroke studies to have intrinsic contrast blood flow signals without introducing exogenous agents into the system. Laser speckle contrast imaging (LSCI) is a label-free technique that utilizes dynamic light scattering to visualize blood flow [26], providing

measurements of relative flow velocity across a large FOV. However, LSCI suffers from limited spatial resolution, and lacks depth-resolved information.

Optical coherence tomography (OCT) [27] is an promising optical imaging modality that enables three-dimensional (3D) volumetric imaging of biological tissue microstructure. OCT angiography (OCTA) [28] is the application of OCT for measuring and visualizing 3D mapping of blood perfusion, achieved by mathematically analyzing the red blood cells' motion-induced temporal changes of scattering signals. For the brain or retina, early lesions are often challenging to be detected. If OCT is used for structural observation, the lesion can only be observed when the condition deteriorates to the point where structural changes occur, which is too late. Fortunately, early lesions often manifest first in alterations to the vascular network, such as strokes in the brain, diabetic retinopathy and age-related macular degeneration in the retina. OCTA is an excellent solution for detecting changes in vascular networks. If we can detect these changes early when the vascular network is affected, we can intervene promptly to prevent further deterioration. Compared with other optical techniques, OCTA allows rapid, high-sensitivity, contrast-free imaging with micron-scale resolution, making it a promising choice for large field of view applications like stroke monitoring [8].

However, for high-resolution optical imaging, the pursuit of diffraction-limited resolution is often accompanied by a trade-off in the form of a reduced DOF, resulting in a degradation of lateral resolution beyond the optical focal plane. This constraint impedes rapid acquisition of high-resolution images of samples with irregular surfaces. Imaging such tissues usually involves laborious axial scanning at multiple planes and complicated image processing procedures. Furthermore, for time-sensitive applications like intraoperative histology or cerebral hemodynamics, rapid high-resolution imaging of irregular surfaces along a large DOF is incredibly desirable. Consequently, numerous approaches have been attempted to enable high-resolution, large DOF imaging. Multi-beam structures [29] can achieve a larger DOF by simultaneously focusing on different depths of the sample, but require complex hardware and software implementations. Additionally, non-diffracting beams such as Bessel [30–33] or Airy [34] beams can achieve large DOF and high resolution, but the imaging quality is usually limited by the severe sidelobes and low beam efficiency. In most studies, axicons are used to generate Bessel beams, which leads to a significant intensity loss during backward light propagation, as a result, additional optical components are necessary to decouple the illumination and detection pathways, which further complicates the system and results in a reduction of the depth of field. Researchers have proposed the use of multi-mode optical fibers to generate coaxially focused multimode beams, achieving high-resolution endoscopic imaging with a 400 μm DOF [35]. In recent years, deep learning models have been used to improve the DOF [36, 37], but this requires a large amount of ground truth during training, and obtaining such data may be challenging or infeasible for certain subjects.

To improve 3D resolution in an optical microscope, we developed a needle-shaped beam (NB), demonstrating its superiority in cellular level OCT imaging of human skin [38], and furthermore, successfully applied it to PAM systems [21]. In this work, we developed a brain vascular level NB-OCTA system that, for the first time, achieved a volumetric resolution of less than 8 μm in a non-stitched volume space of 6.4 mm × 4 mm × 620 μm. Compared to normal OCTA using Gaussian beam

(GB-OCTA), NB-OCTA captures the distribution of blood vessels within a 3.4-times larger depth range. We then employed NB-OCTA to perform long-term in vivo observation of cortical blood perfusion after PT stroke, and quantitatively analyzed the VAD and the diameters of representative vessels in different regions over 10 days, revealing the dynamic spatial and temporal evolution of post-thrombotic blood flow perfusion. Benefiting from our NB-OCTA, we revealed that the recovery process is not only the result of spontaneous reperfusion, but also the formation of new vessels. This study provides a powerful monitoring tool for therapeutic investigations and drug screening for strokes, and deepens our understanding of the mechanisms of ischemic injury and subsequent revascularization in stroke.

Results

The principle of NB-OCTA

An NB is composed of numerous closely adjacent foci along the axial direction, which are generated by a customized diffractive optical element (DOE) and a corresponding objective [38]. The beam length can be flexibly adjusted by increasing or decreasing the number of foci. The DOE phase is formulated as

$$P_{DOE}(x,y) = \sum_{m=1}^{M} \left\{ \left[-\pi n \left(x^2 + y^2 \right) (1/f_m - 1/f)/\lambda - 2\pi mA \right] Loc_m(x,y) \right\} \quad (1)$$

where (x, y) is the planar coordinate, λ is the wavelength, f is the focal length of the objective, n is the refractive index of the surrounding medium, M is the foci number, m is the focus index, $Loc_m(x, y)$ is a binary matrix whose value is either 0 or 1 to identify whether the pixel is allocated to the focus f_m, $2\pi mA$ is the phase regulator for adjusting the beam diameter, and the item $[-\pi n(x^2 + y^2)(1/f_m - 1/f)/\lambda - 2\pi mA]$ aims to shift the focus from f to f_m. The DOE pixels are equally and randomly allocated into m subsets (Fig. 1a). f_1 was set to be coincident with the objective lens focus f, the beam length is determined by $(f_m - f_1)$. When designing the needle-shaped beam, the first consideration is the desired depth of focus. Based on the wanted length, we determine the number of focal points, following the principle that the distance between adjacent focal points should be less than the Rayleigh length (usually 0.5–0.8 times Rayleigh length). However, we found that overlaying the phases of multiple foci leads to uneven axial intensity. To address this, the positions of the foci need to be optimized. We calculate the optimized axial intensity distribution using Fresnel diffraction, and further adjust the spacing between adjacent foci based on the current intensity distribution. After this iterative optimization process, we obtain a beam with uniformly distributed axial intensity. In this work, we designed two NBs for different scenarios, one being 420 μm long with a diameter between 6.5 ± 0.5 μm and the second being 620 μm long with a diameter between 7.4 ± 0.6 μm. The first NB is composed of 49 foci with a phase modulator A of 0.01, while the second contains 81 foci with $A = 0.008$. We didn't make the DOF to be particularly long due to considerations of axial light intensity. In OCTA applications, sensitivity cannot be enhanced through coherent averaging like in OCT imaging, so the intensity of the beam must be sufficient to detect the flow of red blood cells. Therefore, we chose a balance between DOF gain and beam intensity to achieve good angiographic results.

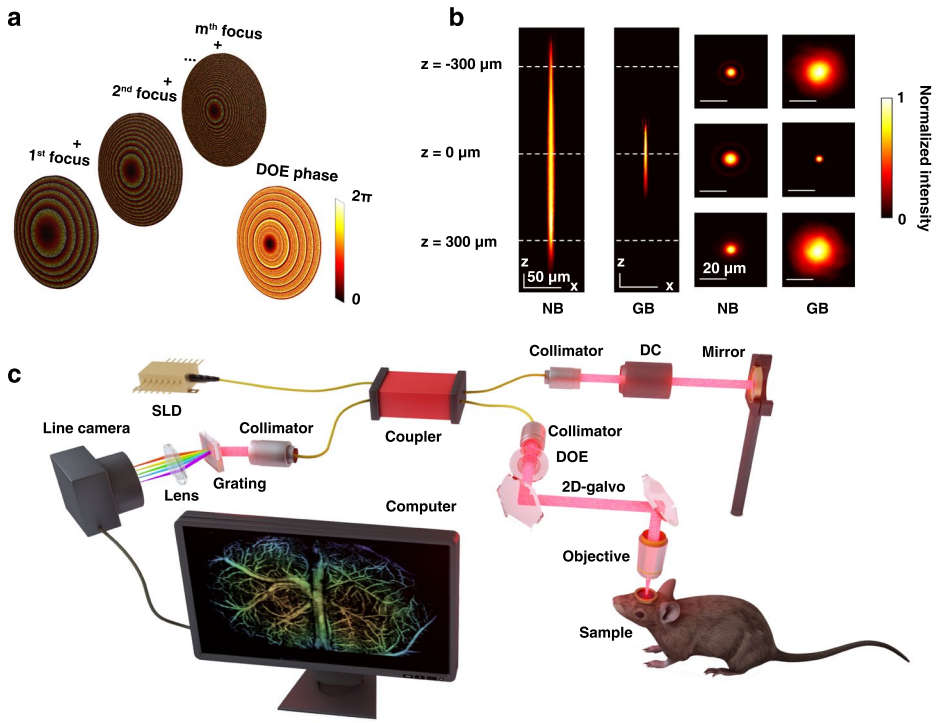

Fig. 1 Principle of NB-OCTA with a customized DOE. **a** DOE phase pattern for an NB composed of multiple phases to generate *m* foci. **b** x–z (left two) profiles of a 620 μm NB generated by DOE and the Gaussian beam generated solely by the objective. And x–y (right two) profiles of the NB and GB at different depth positions. **c** Experimental setup of the NB-OCTA system, with customized DOE in the sample arm. DC, dispersion compensator

The profiles of Gaussian beam and 620 μm NB are compared in Fig. 1b. We define the beam length as the range in which the spot size is smaller than 8 μm. The Gaussian beam has a 4 μm (full-width-at-half-maximum, FWHM) diameter size at the focal plane, expanding to 8 μm in the axial range of 180 μm. The NB achieves a minimal spot size of 6.8 μm, remaining smaller than 8 μm across a depth range of 620 μm. The NB's consistent spot size is demonstrated across three axial positions (z = -300 μm, z = 0 μm, z = 300 μm). Note the NB is tapered, with narrower edges and a thicker center. Contrastingly, the Gaussian beam has the smallest spot size centered at the focal plane. With a DOE, we achieved a maximum efficiency of 30%, which means that the energy enclosed in the main lobe is 30% of the GB focal spot energy. Compared to Bessel beam whose sidelobe-to-main-lobe ratio can be up to 20%, our NB can be optimized to be less than 3%, eliminating the need for complicated image processing in NB-OCTA. The DOE was easily installed in the sample arm before the galvo mirror and objective lens (Fig. 1c), without requiring modifications to the original system (details shown in Fig. S1).

To acquire OCTA signals, intensity information from consecutive B-scans at the same spatial position is compared. Static tissue produces consistent intensity, while the movement of red blood cells through vessels produces intensity variations. By subtracting the intensity values of the consecutive B-scans, the OCTA algorithm

selectively enhances the changes caused by blood flow while suppressing the static signals.

NB-OCTA system performance

The focused Gaussian beam and two NBs were tested with 5 μm polystyrene (PS) beads (XFJ100, XFnano) embedded in ultrasound gel (Ultrasonic Coupling, Cofoe). The phantom with beads concentration around 2×10^5 /mm^3 was degassed with a centrifuge (10 min at 15 000 rpm, H1850, Cence). The B-scan image acquired by the GB only showed recognizable beads only near the focal plane, while areas far from the focus displayed significant blurring, Fig. 2a. For 420 μm NB, particles can be distinguished across a wider range, while the 620 μm NB could distinguish particles wider still. Figure 2b shows x–y planes at five depths. At z = 0, all three beams can distinguish beads clearly. For 620 μm NB, a 21% sidelobe ratio appears, note that this number is not the beam sidelobe ratio, it's read from the logarithmic scale image after data processing, but in the dense bio-samples, the sidelobe effect can be limited, as demonstrated in the following experiments. At z = ± 210 μm, Gaussian beam beads profiles deform significantly, while

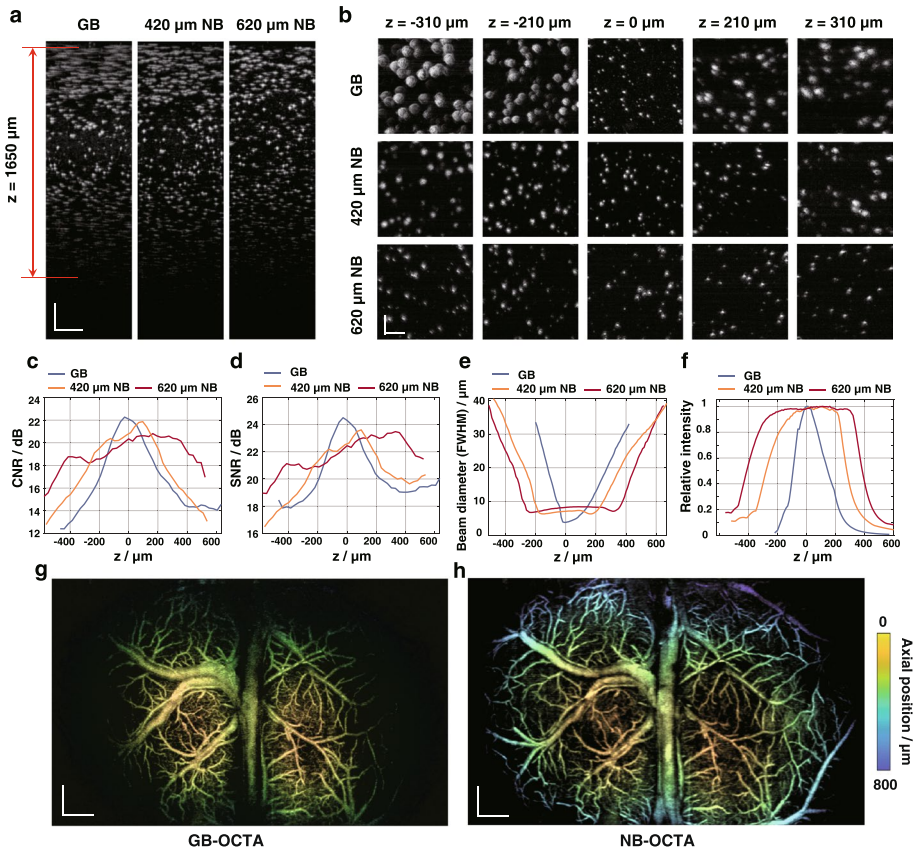

Fig. 2 OCTA system performance with GB and NB.**a** OCT B-scan (x–z) images of 5 μm microbeads by GB, 420 μm NB and 620 μm NB, scale bars at bottom left, 200 μm. **b** OCT *En face* (x–y) images of 5 μm microbeads at five depths, scale bars at bottom left, 100 μm. **c** Contrast-to-noise ratios (CNRs) and(**d**) Signal-to-noise ratios (SNRs) of (**b**) along the depth. **e** Diameters of the used GB, 420 μm NB and 620 μm NB. **f** Relative intensity of the used GB, 420 μm NB and 620 μm NB. **g** and **h** in vivo non-stitching, depth-encoded OCTA images of mouse brain (6.4 mm × 4 mm) acquired by GB and 620 μm NB, respectively. Scale bars at bottom left, 500 μm

420 μm and 620 μm NBs maintain clarity. At z = ± 310 μm, only the 620 μm NB provides high-quality images. About the slight distortions of the beads at z = -210 and -310 um of the GB panel, there are two reasons that can explain: First, the position of the galvanometer mirrors was not perfectly aligned, causing a slight deviation between the beam's emission direction and the system's optical axis. Second, these images are obtained from a single depth pixel layer, where particles may appear as ellipses. Complete data of large scanning area and at more given depth can be found in Supplementary information Figs. S3, S4. The contrast-to-noise ratios (CNRs) along the depth and the signal-to-noise ratios (SNRs) along the depth are shown in Fig. 2c and d. Here, CNR = (average signal intensity- average background intensity)/standard deviation of background intensity, SNR = average signal intensity/ standard deviation of background intensity. We demonstrate the contrast and sensitivity of NB stay relatively stable within the designed beam lengths, and furthermore, NBs outperform the focused Gaussian beam in the depths far from the focal plane. The beam diameter and relative intensity shown in Fig. 2e and f were measured by a microscope system together with a beam profiler (BP209IR1, Thorlabs) with 10 μm as the axial scanning step size (experimental setup shown in Fig. S2), by adjusting the axial positions of the foci, we can achieve a relatively uniform axial intensity, with uniformity higher than 90% in the target region.

OCTA has been widely used for retinal and cerebral vascular imaging. However, the large curvature of the mouse brain cortex makes it challenging for conventional GBs to cover the entire region due to its limited DOF. Consequently, generating a large-field brain vascular image [8, 39] has previously required stitching multiple small FOVs, which fundamentally prohibits simultaneous imaging of the entire cortical vasculature, and introduces significant complexity and uncertainty in FOV merging during image processing. Using NB-OCTA, we collected in vivo, non-stitched, large field of view (6.4 mm × 4 mm) images of the mouse brain (Fig. 2g and h). To better visualize the brain's curvature, we encoded the depth with colors. Conventional GB-OCTA could image the small vessels within its focal range, but missed many vessels in the surrounding lower periphery. In contrast, NB-OCTA clearly resolved more vessels around the margins and could image the entire 800 μm depth range. The brain was scanned five times using 58.5 s, with a fast-axis scanning step of 8 μm, and a slow-axis scanning step of 5 μm.

Quantitative comparison between GB-OCTA and NB-OCTA

Before monitoring cerebral stroke, we imaged the selected area using both GB-OCTA and NB-OCTA. This region, situated on the left side of the mouse brain's sagittal suture, exhibited a depth difference of 450 μm between the left and right sides due to the brain's natural curvature. This height difference exceeded the DOF of most high-resolution OCTA systems. Traditional solution is to rotate the sample or the probe to align the Gaussian beam perpendicular to one subregion of sample surface [39], capture image of that region, and then rotate to the next. This process is repeated multiple times and the images are stitched together to minimize defocusing. However, this method is time-consuming and requires software and hardware coordination, thus being inconvenient during rapid imaging. In contrast, our proposed NB has a focal depth larger than the height difference of the sample surface, enabling direct

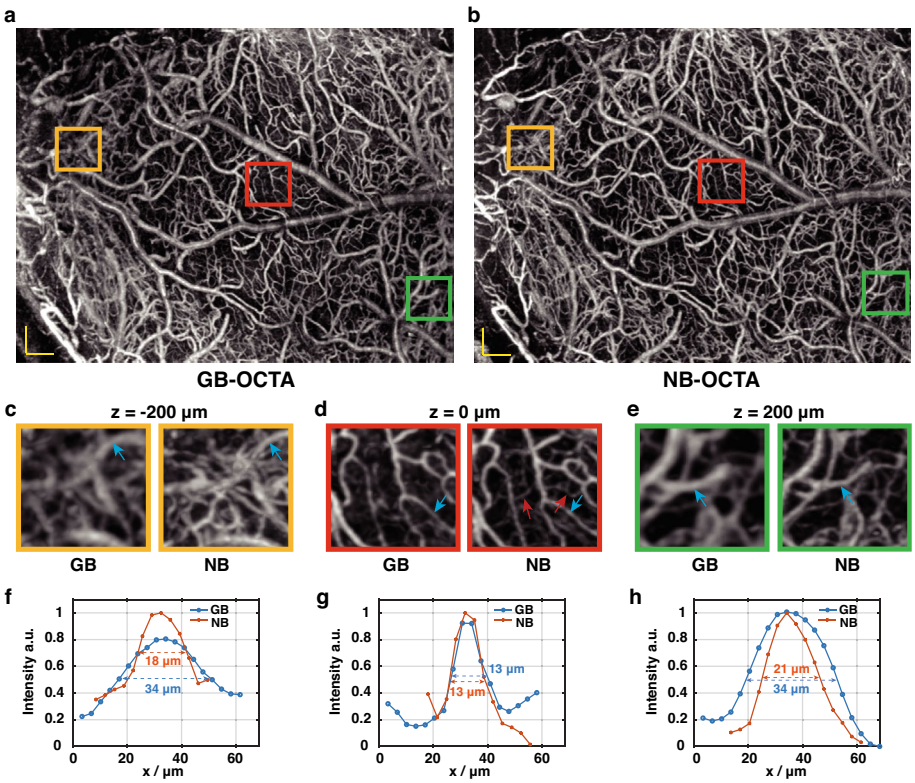

Fig. 3 In vivo OCTA imaging of curved sections of mouse brain (2.5 mm × 3.1 mm) with GB and NB. **a***En face* (x–y) image acquired by GB-OCTA, scale bars at bottom left, 200 μm. **b***En face* (x–y) image acquired by NB-OCTA. The yellow, red, and green boxes in (**a** and **b**) are zoomed in as (**c**, **d**, and **b**), indicating axial positions of -200 μm, 0 μm, and 200 μm, respectively. The images are defocused in yellow and green boxes with GB but not with NB. The red boxes are within the depth of focus of both GB and NB, but with higher CNR, some micro vessels are visible in NB image but not in GB image, marked by red arrows. **f**, **g**, and **h** The profiles of a single micro vessel (marked by blue arrows) in (**c**, **d**, and **e**) respectively

high-resolution imaging of the selected region without the need for rotation. Figure 3a and b show OCTA images obtained with GB and NB, respectively. Comparing these images, the GB-OCTA image exhibits blurriness on the left and right sides due to defocusing, while the NB-OCTA image maintains high resolution. We zoomed in on three selected regions at depths of z = -200 μm, 0 μm, and 200 μm, Fig. 3c, d, and e. Profiles of selected single vessels (indicated by blue arrows) were drawn in Fig. 3f, g and h, respectively. Outside the DOF of GB (yellow and green boxes), vessels in the GB-OCTA image appear widened, whereas the NB-OCTA image remains unaffected. In the central region (red boxes), both GB-OCTA and NB-OCTA were able to provide a high-resolution image, Fig. 3d, and the selected blood vessel diameter was measured to be the same in both modalities, Fig. 3g. However, as light penetrates deeper into the tissue, the Gaussian beam apparently defocused, resulting in weaker light intensity and larger beam size at the current scanning point, which increased noise. Consequently, some micro blood vessels can only be visualized in NB-OCTA, red arrows in Fig. 3d.

In addition, we also calculated CNR, SNR, and vessel connectivity to quantitatively evaluate the image quality of Fig. 3a and b. In Fig. 3a, the CNR, SNR, and vessel connectivity were 16.8 dB, 17.7 dB, and 54.8%, respectively, while in Fig. 3b, they were 20.6 dB,

22.1 dB, and 73.7%, respectively. The connectivity is defined as the ratio of the biggest number of connected pixels and the total number of pixels that refers to vessels. Higher CNR helps to accurately distinguish blood vessels from surrounding tissues, while higher SNR improves image clarity and visibility of details, aiding in the accurate assessment of vessel connectivity.

To further demonstrate that the GB is not suitable for this scenario, we present experimental results of focusing at multiple z-positions, see Figs. S5, S6 in Supplementary. The results show that no matter where the focus is, the DOF of the GB cannot cover the height difference of the sample surface, so there would always be positions out of focus. Based on the experimental results above, NB-OCTA was employed to monitor the whole process of the recovery from PT stroke.

Long-term observation of blood perfusion after stroke with NB-OCTA

NB-OCTA can overcome the natural curvature of the mouse brain and achieve fast high-resolution imaging, making it an ideal tool for monitoring blood thrombosis. Figure 4 illustrates the entire process in mouse cerebral vasculature from acute ischemia to

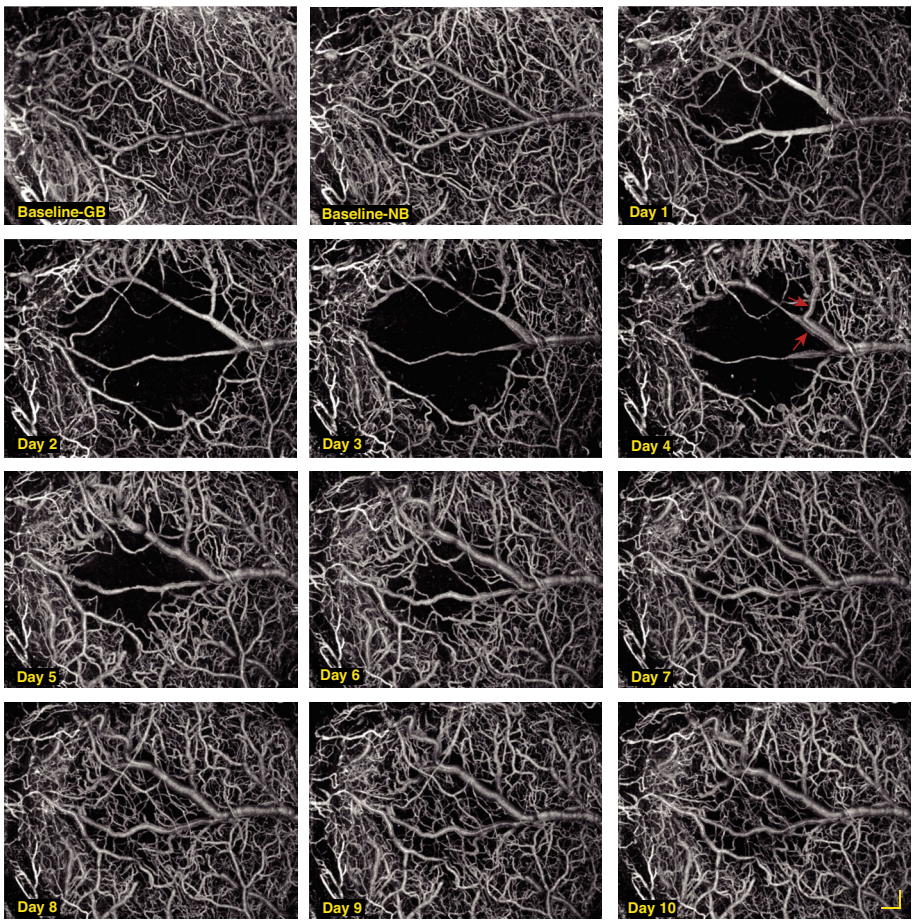

Fig. 4 Dynamic blood flow observation after PT stroke by NB-OCTA. The first image is taken before the thrombosis was induced, followed by 1- 10 days after stroke, this is a process from acute ischemia to chronic recovery, field of view, 2.5 mm × 3.1 mm. Scale bars at bottom right, 200 μm

chronic recovery following PT stroke induction. The first two images illustrate a baseline prior to PT induction with GB and NB. After the PT stroke was induced, a focal ischemic area was formed. On the first day after PT induction (30 min post-induction), partial loss of blood flow signals was observed. In the following two days, the ischemic area expanded significantly, with the vascular network in the core region disappearing remarkably. Around the fourth day, the vascular network began to recover and the ischemic region began to shrink. Some blood vessels that had disappeared due to blockage reappeared due to spontaneous recanalization. In addition, the diameters of large blood vessels in the core area (indicated by red arrows) expanded significantly, possibly to compensate for other blocked vessels. On the fifth and sixth days, the area of the core ischemic region continued to shrink, and more blocked small blood vessels spontaneously reperfused. Starting from the seventh day the ischemic area tended to stabilize, and the expanded blood vessels due to compensation effects also began to regress. However, compared with the baseline image before the thrombosis, some deep capillaries did not reperfuse.

In addition, we quantitatively analyzed the entire process as shown in Fig. 5. The core ischemic area, denoted by the red circle, encapsulated the vast majority of the ischemic tissue, while the area outside the red circle was defined as the peripheral area. We

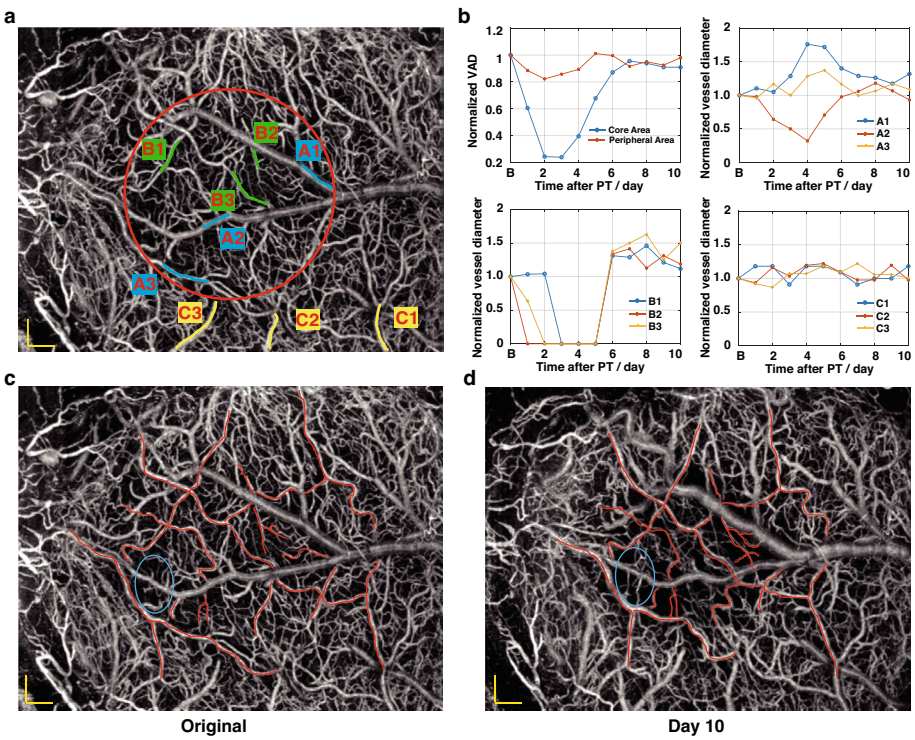

Fig. 5 Quantitative analysis of dynamic blood flow changes. **a** Introduction of the selected area (circled by red) for VAD analysis, and three representative vessels from group A, B and C for diameter changes analysis. Group A: Vessels that did not get blocked or did not disappear during the long-term monitoring, but were from the core area. Group B: Vessels that got blocked and disappeared from the core. Group C: Vessels from the periphery. **b** VAD analysis and vessel diameter changed analysis, normalized to the normal state. Core area: inside the red circle in (**a**) peripheral area: outside the red circle in (**a c** and **d**) Comparison between the normal state and 10 days after stroke. Red lines: the same vessels which can be manually identified. Blue circle in (**d**) newly generated vessels that cannot be found in the same area in (**c**) Scale bars at bottom left, 200 μm

conducted a long-term analysis of VAD in two regions, and, as shown in Fig. 5b, the VAD in the core area dropped sharply at first, then began to recover on the fourth day and stabilized after the seventh day. The VAD of the peripheral area was relatively stable with small fluctuations, which was consistent with the intuitive results of Fig. 4. We also selected three representative blood vessels of three groups to analyze the diameter changes during the whole process, shown in Fig. 5b. Group A is composed of vessels from the core area that did not disappear or were not blocked. The diameter of these vessels changed over the course of the experiment. Vessel A2 was partially blocked and then recovered. Vessel A1 and A3 got widened, which indicates they did more transportation work to compensate for the blocked vessels. Following the reperfusion of these blocked vessels, A1 and A3 returned back to their normal state. Group B consists of vessels that were blocked and disappeared from the core, but then reperfused spontaneously. Group C is comprised of the vessels from the periphery. These vessels were relatively stable, and do not have obvious diameter changes, indicating that the peripheral vessels were not significantly affected. This further supports the advantages of the PT model in terms of its precision and controllability.

Additionally, by comparing the spatial location of the reperfused flow with the original vessels (Fig. 5c and d), we believe that the recovery process is not only the result of spontaneous reperfusion (indicated by the red lines), but also the formation of new vessels, as indicated by the blue oval area in Fig. 5d. While currently the difference is manually identified, more compelling evidence about angiogenesis can be obtained through molecular experiments such as the Western blotting for angiogenic markers such as VEGF and its fms-like tyrosine (FLT) kinase receptor [40].

Discussion

In this work we have designed and demonstrated a novel NB-OCTA system featuring a substantially improved field of view and DOF compared to conventional GB-OCTA systems. This system enables, for the first time, a volumetric resolution of 8 μm across a non-stitched volume space of 6.4 mm × 4 mm × 620 μm. The NB's elongated DOF enables rapid high-resolution imaging across the brain's curved surface, something previously impossible without time-consuming Z-stacking and laborious image compiling. Note that the current improvements of DOF are not the theoretical limit, which can be further adjusted according to the laser energy and required efficiency of the system. In addition, we demonstrated 10 days observation of blood perfusion after stroke with NB-OCTA, revealing distinct spatiotemporal dynamics in the acute, sub-acute and chronic phase of post-ischemic revascularization. Our experiment displays the initial three days following PT occlusion can be considered as the acute phase of vessel thrombosis, during which the VAD decreased gradually, resulting in peak ischemia area on day 3. Subsequently, the blood flow began to recover from the peripheral region towards the ischemic core, and from the seventh day onwards, the ischemic area tended to stabilize. Furthermore, the NB-OCTA has demonstrated the recovery process is not only the product of spontaneous reperfusion, but also the formation of new vessels. During the whole process, blood perfusion is changing in real-time, when using GB-OCTA to observe this process on a large FOV, the need for image stitching results in slower

imaging speeds. Therefore, the stitched images do not represent the exact same moment of acquisition, which can impede clinicians and researchers in making judgments about the thrombus status.

NB-OCTA holds a fundamental advantage over traditional GB-OCTA by enabling rapid imaging without scanning and stitching of subregions, which was previously impossible for samples with uneven surfaces. Real-time imaging is beneficial for operation navigation and monitoring during the surgical process [41]. With the assistance of GPU [42], NB-OCTA can provide high-resolution real-time cross-section images and rapid 3D volumetric data during surgery. We believe this can assist doctors in accurately locating lesion areas and organ structures, such as determining the range of tumor resection, which may help to maximize the preservation of normal tissue and enables doctors to make quick and precise decisions during surgery.

NB-OCTA shows promise across multiple applications, potentially enabling novel functions and providing improved imaging performance. For example, by combining NB-OCTA with Doppler technology [43], it is possible to measure blood flow velocity in deep vessels. Furthermore, contrast agents [44] can alleviate the energy attenuation caused by the efficiency and elongation of the beam in NB-OCTA. NB-OCTA can also be used to guide and observe micro and nano robots [45], making it potentially suitable for targeted drug delivery and minimally invasive surgery.

In addition, technological improvements of NB-OCTA can extend its applications, expanding its relevancy across medical and biological research. NB-OCTA can benefit from adaptive optics technology to correct wavefront distortions caused by tissue heterogeneity, thereby obtaining higher-contrast and higher-resolution images [46]. Combining NB-OCTA with other imaging modalities can provide complementary information [47], allowing analysis beyond the sum of the individual parts. For example, combining NB-OCT(A) with photoacoustic imaging can provide functional information about tissue oxygenation and blood flow as well as high axial resolution cross-section images [48], making diagnosis and monitoring of disease progression more accurate. Furthermore, artificial intelligence (AI) algorithms can both improve image quality and make analysis and diagnosis [49], reducing the workload of clinical doctors and improving the accuracy and reliability of diagnosis.

Conclusion

Our study provides a new approach for developing optical microscopy systems with consistently high spatial resolution and contributes to a better understanding of the mechanisms of ischemic injury and revascularization in stroke. Furthermore, we believe that NB-OCTA has great potential for a broader range of applications in the future by combining with other technologies.

Materials and methods

DOE fabrication

The phase mask was created on a DOE which was fabricated on a 500-μm-thick fused silica wafer via four rounds of lithography. The relationship between the phase modulation $P(x, y)$ and the height $H(x, y)$ of the DOE can be expressed as

$$P(x,y) = \frac{2\pi(n_{DOE} - 1) \cdot H(x,y)}{\lambda} \tag{2}$$

where n_{DOE} is the refractive index of the material and λ is the wavelength. For fused silica, n_{DOE}=1.453 at 850 nm, and the incremental thickness is 117 nm (π / 8 in phase) for the 16 height levels. The first round of etching is to finish 8×117 nm, the second for 4×117 nm, the third for 2×117 nm and the fourth for 117 nm, combing to generate 16 heights. Each DOE has 1024×1024 pixels, with a 10-μm pixel resolution. The fabrication process was completed at the Stanford Nanofabrication Facility, and the detailed procedure can be found in our previous work [21, 38]. It takes approximately 10 h to manufacture one batch of DOEs, considering all the time costs. The fabrication process achieves a height accuracy better than 95%, and the alignment error for the four rounds of photolithography is around 1 μm.

NB-OCTA system

A homebuilt SD-OCTA, as shown in Fig. 1c was used for imaging with a light source of broadband super luminescent diode (SLD-371HP3, Superlum, 850 ± 25 nm, 15mW), giving an axial resolution of 6.4 μm. The light from the SLD passes through and a 2×2 coupler and is divided into the reference arm and sample arm. We placed the DOE in the sample arm before the objective lens (LSM02BB, Thorlabs, focal size = 5.8 μm), converting the conventional Gaussian beam-OCTA system to an NB-OCTA system. A dispersion compensation unit (LSM02DC, Thorlabs) was used in the reference arm to minimize the dispersion mismatch between the sample arm and the reference arm. The reflected reference light and sample light are combined through the coupler, and a home-built spectrometer with 0.05 nm resolution, 2048 pixel, and 70 kHz maximum A-scan rate is used to record the interference fringes.

Animal preparation

All procedures involving mice were approved by the Institutional Animal Care and Use Committee of Tsinghua University. Wild-type mice (C57BL/6, 9 weeks to 3 months old; weight, 20-30 g) were used in all the in vivo experiments.

We performed the craniotomy surgery as follows: First, mice were anesthetized using isoflurane (3% for induction, 1.5% during surgery), then a toe pinch procedure was conducted to verify the status of anesthesia. After confirming the animal's anesthesia status, the mouse was transferred onto a stereotactic frame with its body temperature maintained by using a heating pad. Before the surgery, ophthalmic ointment was topically applied to the corneal surfaces to prevent corneal drying and damage from prolonged exposure to the illuminating light source. An incision was made in the scalp and craniotomy was performed with a drill [50]. After the skull was removed, the exposed brain was protected during the procedure from drying and infection. For acute experiments (Fig. 2g and h), the brain was covered with 2% low gelling temperature agarose (A4718, Sigma-Aldrich), and Phosphate-buffered saline (PBS) was used instead of water to dissolve the agarose to achieve the same osmotic pressure. A custom aluminum head post was then fixed to the skull using dental cement. For chronic imaging experiments

(Fig. 3-Fig. 5), the brain was covered with 2% agarose and then a cover glass (0.17 mm thickness, 6 mm diameter) was glued to the skull to reduce motion of the exposed brain, and also a custom aluminum head post was fixed to the skull using dental cement. Imaging experiments were started ~ 1–2 weeks after chronic window implantation.

Photothrombotic vascular occlusion

After the mice recovered from the craniotomy surgery, PT occlusion was induced as follows: Rose Bengal (Sigma-Aldrich) solution (2.5 mg/100 g, 7.5 mg/mL) was intraperitoneally injected into the mouse, and then the mouse was allowed to rest for 30 min to allow the solution to be absorbed into the systemic circulation. Then the occlusion was induced by focal illumination (1 mm diameter focal spot, 30 mW/mm^2) with 532 nm laser (MSL-III-532, CNI) in the somatosensory cortex region of the left cerebral hemisphere of the mouse brain for 30 min [8]. After PT occlusion was induced, we acquired OCTA data and then returned the mouse to its cage, where it had free access to food and water. After 24 h, the mouse was anesthetized again for OCTA data acquisition. The experiment lasted for ten days, during which data collection was performed at a consistent time every day.

Data acquisition and processing

In this work, a stepwise raster scanning protocol was used to acquire volumetric dataset, the slow scanner (*y*) was driven by a step waveform with a total of 800 steps, at each step, five repeated B-scan were successively acquired for analyzing dynamic flow signals, with each B-scan composed of 1024 A-lines in the fast-scanning direction. Adjacent B-scans were paired for blood flow extraction at each scanning step *y*. The raw spectral interference fringe signal *S (k, x, t)* was Fourier transformed along the wavenumber direction to produce the backscattered profile *C (z, x, t)* in the depth space, which consists of amplitude and phase information:

$$C_{OCT}(z,x,t) = I(z,x,t)e^{-i\Phi(z,x,t)} \tag{3}$$

The cross-sectional angiogram was then created by subtracting the amplitude component *I (z, x, t)* between paired B-scans:

$$OCTA = |I(z,x,i) - I(z,x,i+1)| \tag{4}$$

Then the OCTA signals at each step y were averaged to improve flow contrast. Performing this process for all y values, OCTA volumetric data containing microvasculature flow information can be obtained. The *en face* angiograms are obtained by performing full-depth maximum intensity projection (MIP) along the axial direction.

The depth-resolved image was color-encoded by assigning depth information to the hue channel, the 2D *en face* image to the value channel, and a constant value to the saturation channel. Subsequently, the color-encoded image was converted from HSV space to RGB space.

In order to assess the quality of the *en face* OCTA images acquired by GB and NB, several parameters were evaluated, including contrast-to-noise ratio (CNR), signal-to-noise ratio (SNR), and vessel connectivity. Prior to analysis, the *en face* OCTA images were normalized and converted to binary format by applying a threshold to differentiate blood vessels from

static tissues, a skeleton map (M) was then generated. The CNR and SNR were calculated according to the following definitions:

$$CNR_{en\ face\ OCTA} = \frac{\overline{I(x,y)|_{M(x,y=1)}} - \overline{I(x,y)|_{Bck}}}{\sigma_{I(x,y)|Bck}} \tag{5}$$

$$SNR_{en\ face\ OCTA} = \frac{\overline{I(x,y)|_{M(x,y=1)}}}{\sigma_{I(x,y)|Bck}} \tag{6}$$

where $\overline{I(x,y)|_{M(x,y=1)}}$ is the mean value of the intensities of the pixels that corresponded to the skeleton map in the *en face* OCTA image, $\overline{I(x,y)|_{Bck}}$ represents the average intensity of pixels in the background (tissue) area of the *en face* image, and $\sigma_{I(x,y)|Bck}$ is the standard deviation of the background signals.

The connectivity is defined as the ratio of the biggest number of connected pixels and the total number of pixels that refers to vessels.

Abbreviations

DOF	Depth of Field
OCT	Optical Coherence Tomography
NB-OCTA	Needle-Shaped Beam Optical Coherence Tomography Angiography
GB-OCTA	Gaussian Beam Optical Coherence Tomography Angiography
VAD	Vessel Area Density
PT	Photothrombotic
VEGF	Vascular Endothelial Growth Factor
MRI	Magnetic Resonance Imaging
CT	Computed Tomography
PAM	Photoacoustic Microscopy
2PM	Two-Photon Microscopy
LSCI	Laser Speckle Contrast Imaging
DOE	Diffractive Optical Element
PS	Polystyrene
CNR	Contrast-To-Noise Ratio
SNR	Signal-To-Noise Ratio
FLT	Fms-Like Tyrosine
PBS	Phosphate-Buffered Saline

Supplementary Information

The online version contains supplementary material available at https://doi.org/10.1186/s43074-024-00124-9.

Supplementary Materials1.

Acknowledgements

We thank Yang Lin and Xiaochen Li for helping with bio-sample preparation and discussing for data processing.

Authors' contributions

X.G. and J.Z. designed the experiments. X.G. and L.S. performed system integration and calibration. J.Z. designed and fabricated the DOEs. L.D. contributed to the mask preparation and wafer dividing. X.G. and J.Z conducted performance optimization. L.K. prepared the animals and supervised the biological experiments. X.G performed the imaging experiments. V.G. and K.S. contributed to stroke model processing and data analysis. X.G., J.Z., L.S. and Y.H. contributed to image processing. A.V.V. and K.L. contributed to editing of the manuscript. L.C. and Y.Y. contributed to the optimization of system design. G.J., A.d.l.Z. and Y.H. supervised the project. All authors provided critical revision feedback to the manuscript.

Funding

This work was supported by the National Key R&D Program of China (No.2022YFB4702902), National Natural Science Foundation of China (Nos. 61831014, 62275023, and 32021002), Beijing Municipal Natural Science Foundation (No. 4232077), Overseas Expertise Introduction Project for Discipline Innovation (No. B18005), STI2030-Major Projects (No. 2022ZD0212000).

Availability of data and materials

All data needed to evaluate the conclusions in the paper are present in the paper and/or the Supplementary Materials. Additional data related to this paper may be requested from corresponding authors.

Declarations

Competing interests
The authors declare no competing interests.

Author details
[1]State Key Laboratory of Precision Measurement Technology and Instruments, Department of Precision Instrument, Tsinghua University, Beijing 100084, China. [2]Department of Structural Biology, Stanford University School of Medicine, Stanford University, Stanford, CA 94305, USA. [3]Department of Neurosurgery, Stanford University School of Medicine, Stanford University, Stanford, CA 94305, USA. [4]Department of Radiology, Stanford University School of Medicine, Stanford University, Stanford, CA 94305, USA. [5]Department of Electrical Engineering and Computer Sciences, University of California, Berkeley 94720, USA. [6]School of Optics and Photonics, Beijing Institute of Technology, No. 5 South Zhongguancun Street, Haidian, Beijing 100081, China. [7]Biophysics Program, Molecular Imaging Program, and Bio-X Program at Stanford University, Stanford, CA 94305, USA. [8]Chan Zuckerberg Biohub, San Francisco, CA 94110, USA. [9]Institute of Medical Equipment Science and Engineering, Huazhong University of Science and Technology, Wuhan 430074, China.

Received: 8 November 2023 Revised: 7 February 2024 Accepted: 13 March 2024
Published online: 27 March 2024

References

1. Campbell BC, De Silva DA, Macleod MR, Coutts SB, Schwamm LH, Davis SM, et al. Ischaemic stroke Nature Reviews Disease Primers. 2019;5(1):70.
2. Fluri F, Schuhmann MK, Kleinschnitz C. Animal models of ischemic stroke and their application in clinical research. Drug Des Devel Ther. 2015;9:3445.
3. Sommer CJ. Ischemic stroke: experimental models and reality. Acta Neuropathol. 2017;133(2):245–61.
4. Robinson RG, Shoemaker WJ, Schlumpf M, Valk T, Bloom FE. Effect of experimental cerebral infarction in rat brain on catecholamines and behaviour. Nature. 1975;255(5506):332–4.
5. Belayev L, Alonso OF, Busto R, Zhao W, Ginsberg MD. Middle cerebral artery occlusion in the rat by intraluminal suture: neurological and pathological evaluation of an improved model. Stroke. 1996;27(9):1616–23.
6. Kuroiwa T, Xi G, Hua Y, Nagaraja TN, Fenstermacher JD, Keep RF. Development of a rat model of photothrombotic ischemia and infarction within the caudoputamen. Stroke. 2009;40(1):248–53.
7. Lu H, Li Y, Yuan L, Li H, Lu X, and Tong S. Induction and imaging of photothrombotic stroke in conscious and freely moving rats. J. Biomed. Opt. 2014;19(9):096013-
8. Yang S, Liu K, Ding H, Gao H, Zheng X, Ding Z, et al. Longitudinal in vivo intrinsic optical imaging of cortical blood perfusion and tissue damage in focal photothrombosis stroke model. J Cereb Blood Flow Metab. 2019;39(7):1381–93.
9. Zhang H, Zhao Z, Sun S, Zhang S, Wang Y, Zhang X, et al. Molecularly self-fueled nano-penetrator for nonpharmaceutical treatment of thrombosis and ischemic stroke. Nat Commun. 2023;14(1):255.
10. He L, Huang G, Liu H, Sang C, Liu X, and Chen T. Highly bioactive zeolitic imidazolate framework-8–capped nanotherapeutics for efficient reversal of reperfusion-induced injury in ischemic stroke. Science Advances. 2020;6(12):eaay9751.
11. Murphy TH, Corbett D. Plasticity during stroke recovery: from synapse to behaviour. Nat Rev Neurosci. 2009;10(12):861–72.
12. Molina C A. Reperfusion therapies for acute ischemic stroke: current pharmacological and mechanical approaches. Stroke. 2011;42(1_suppl_1):S16-S9
13. Bhaskar S, Stanwell P, Cordato D, Attia J, Levi C. Reperfusion therapy in acute ischemic stroke: dawn of a new era? BMC Neurol. 2018;18:1–26.
14. Thomalla G, Simonsen CZ, Boutitie F, Andersen G, Berthezene Y, Cheng B, et al. MRI-guided thrombolysis for stroke with unknown time of onset. N Engl J Med. 2018;379(7):611–22.
15. Yanev P, Dijkhuizen RM. In vivo imaging of neurovascular remodeling after stroke. Stroke. 2012;43(12):3436–41.
16. Carmeliet P. Mechanisms of angiogenesis and arteriogenesis. Nat Med. 2000;6(4):389–95.
17. Risau W. Mechanisms of angiogenesis. Nature. 1997;386(6626):671–4.
18. Ruan L, Wang B, ZhuGe Q, Jin K. Coupling of neurogenesis and angiogenesis after ischemic stroke. Brain Res. 2015;1623:166–73.
19. Wang X, Leong AT, Tan SZ, Wong EC, Liu Y, Lim L-W, et al. Functional MRI reveals brain-wide actions of thalamically-initiated oscillatory activities on associative memory consolidation. Nat Commun. 2023;14(1):2195.
20. Tayyebi S, Akhavan R, Shams M, Salehi M, Farrokh D, Yousefi F, et al. Diagnostic value of non-contrast brain computed tomography in the evaluation of acute cerebral venous thrombosis. Sci Rep. 2020;10(1):883.
21. Cao R, Zhao J, Li L, Du L, Zhang Y, Luo Y, et al. Optical-resolution photoacoustic microscopy with a needle-shaped beam. Nat Photonics. 2023;17(1):89–95.
22. Wang T, Xu C. Three-photon neuronal imaging in deep mouse brain. Optica. 2020;7(8):947–60.
23. Zhu X, Huang Q, DiSpirito A, Vu T, Rong Q, Peng X, et al. Real-time whole-brain imaging of hemodynamics and oxygenation at micro-vessel resolution with ultrafast wide-field photoacoustic microscopy. Light: Science & Applications. 2022;11(1):138.
24. Zong W, Wu R, Li M, Hu Y, Li Y, Li J, et al. Fast high-resolution miniature two-photon microscopy for brain imaging in freely behaving mice. Nat Meth. 2017;14(7):713–9.
25. Burgess A, Nhan T, Moffatt C, Klibanov A, Hynynen K. Analysis of focused ultrasound-induced blood–brain barrier permeability in a mouse model of Alzheimer's disease using two-photon microscopy. J Control Release. 2014;192:243–8.

26. Li D-Y, Xia Q, Yu T-T, Zhu J-T, Zhu D. Transmissive-detected laser speckle contrast imaging for blood flow monitoring in thick tissue: from Monte Carlo simulation to experimental demonstration. Light: Science & Applications. 2021;10(1):241.
27. Drexler W, Fujimoto JG. Optical coherence tomography: technology and applications. Springer; 2015.
28. Spaide RF, Fujimoto JG, Waheed NK, Sadda SR, Staurenghi G. Optical coherence tomography angiography. Prog Retin Eye Res. 2018;64:1–55.
29. Standish BA, Lee KK, Mariampillai A, Munce NR, Leung MK, Yang VX, et al. In vivo endoscopic multi-beam optical coherence tomography. Phys Med Biol. 2010;55(3):615.
30. Lorenser D, Singe CC, Curatolo A, Sampson DD. Energy-efficient low-Fresnel-number Bessel beams and their application in optical coherence tomography. Opt Lett. 2014;39(3):548–51.
31. Leitgeb R, Villiger M, Bachmann A, Steinmann L, Lasser T. Extended focus depth for Fourier domain optical coherence microscopy. Opt Lett. 2006;31(16):2450–2.
32. Tamborski S, Lyu HC, Dolezyczek H, Malinowska M, Wilczynski G, Szlag D, et al. Extended-focus optical coherence microscopy for high-resolution imaging of the murine brain. Biomed Opt Express. 2016;7(11):4400–14.
33. Ding Z, Ren H, Zhao Y, Nelson JS, Chen Z. High-resolution optical coherence tomography over a large depth range with an axicon lens. Opt Lett. 2002;27(4):243–5.
34. Zhang M, Ren Z, Yu P. Improve depth of field of optical coherence tomography using finite energy Airy beam. Opt Lett. 2019;44(12):3158–61.
35. Yin B, Hyun C, Gardecki JA, Tearney GJ. Extended depth of focus for coherence-based cellular imaging. Optica. 2017;4(8):959–65.
36. Jin L, Tang Y, Wu Y, Coole JB, Tan MT, Zhao X, et al. Deep learning extended depth-of-field microscope for fast and slide-free histology. Proc Natl Acad Sci. 2020;117(52):33051–60.
37. Wu Y, Rivenson Y, Wang H, Luo Y, Ben-David E, Bentolila LA, et al. Three-dimensional virtual refocusing of fluorescence microscopy images using deep learning. Nat Meth. 2019;16(12):1323–31.
38. Zhao J, Winetraub Y, Du L, Van Vleck A, Ichimura K, Huang C, et al. Flexible method for generating needle-shaped beams and its application in optical coherence tomography. Optica. 2022;9(8):859–67.
39. He B, Zhang Y, Meng Z, He Z, Chen Z, Yin Z et al. Whole Brain Micro-Vascular Imaging Using Robot Assisted Optical Coherence Tomography Angiography. IEEE J. Sel. Top. Quantum Electron. 2022;29(4: Biophotonics):1–9
40. Kovács Z, Ikezaki K, Samoto K, Inamura T, Fukui M. VEGF and flt: expression time kinetics in rat brain infarct. Stroke. 1996;27(10):1865–73.
41. Kut C, Chaichana K L, Xi J, Raza S M, Ye X, McVeigh E R et al. Detection of human brain cancer infiltration ex vivo and in vivo using quantitative optical coherence tomography. Sci. Transl. Med. 2015;7(292):292ra100–292ra100
42. Wei X, Camino A, Pi S, Hormel TT, Cepurna W, Huang D, et al. Real-time cross-sectional and en face OCT angiography guiding high-quality scan acquisition. Opt Lett. 2019;44(6):1431–4.
43. Li Y, Chen J, Chen Z. Advances in Doppler optical coherence tomography and angiography. Translational biophotonics. 2019;1(1–2): e201900005.
44. Nguyen VP, Qian W, Li Y, Liu B, Aaberg M, Henry J, et al. Chain-like gold nanoparticle clusters for multimodal photoacoustic microscopy and optical coherence tomography enhanced molecular imaging. Nat Commun. 2021;12(1):34.
45. Wu Z, Li L, Yang Y, Hu P, Li Y, Yang S-Y et al. A microrobotic system guided by photoacoustic computed tomography for targeted navigation in intestines in vivo. Science robotics. 2019;4(32):eaax0613
46. Camino A, Ng R, Huang J, Guo Y, Ni S, Jia Y, et al. Depth-resolved optimization of a real-time sensorless adaptive optics optical coherence tomography. Opt Lett. 2020;45(9):2612–5.
47. Nguyen VP, Fan W, Zhu T, Qian W, Li Y, Liu B, et al. Long-term, noninvasive in vivo tracking of progenitor cells using multimodality photoacoustic, optical coherence tomography, and fluorescence imaging. ACS Nano. 2021;15(8):13289–306.
48. Hosseinaee Z, Abbasi N, Pellegrino N, Khalili L, Mukhangaliyeva L, Haji RP. Functional and structural ophthalmic imaging using noncontact multimodal photoacoustic remote sensing microscopy and optical coherence tomography. Sci Rep. 2021;11(1):1–11.
49. Varadarajan AV, Bavishi P, Ruamviboonsuk P, Chotcomwongse P, Venugopalan S, Narayanaswamy A, et al. Predicting optical coherence tomography-derived diabetic macular edema grades from fundus photographs using deep learning. Nat Commun. 2020;11(1):130.
50. Chen T-W, Wardill TJ, Sun Y, Pulver SR, Renninger SL, Baohan A, et al. Ultrasensitive fluorescent proteins for imaging neuronal activity. Nature. 2013;499(7458):295–300.

Publisher's Note